

**Lattice Boltzmann model for three-phase viscoelastic fluid flow**

Chiyu Xie, Wenhai Lei, and Moran Wang\*

*Department of Engineering Mechanics and CNMM, Tsinghua University, Beijing 100084, China*

(Received 13 October 2017; published 27 February 2018)

A lattice Boltzmann (LB) framework is developed for simulation of three-phase viscoelastic fluid flows in complex geometries. This model is based on a Rothman-Keller type model for immiscible multiphase flows which ensures mass conservation of each component in porous media even for a high density ratio. To account for the viscoelastic effects, the Maxwell constitutive relation is correctly introduced into the momentum equation, which leads to a modified lattice Boltzmann evolution equation for Maxwell fluids by removing the normal but excess viscous term. Our simulation tests indicate that this excess viscous term may induce significant errors. After three benchmark cases, the displacement processes of oil by dispersed polymer are studied as a typical example of three-phase viscoelastic fluid flow. The results show that increasing either the polymer intrinsic viscosity or the elastic modulus will enhance the oil recovery.

DOI: [10.1103/PhysRevE.97.023312](https://doi.org/10.1103/PhysRevE.97.023312)**I. INTRODUCTION**

Viscoelasticity is one of the most important and toughest topics in rheological properties, since materials with this kind of property exhibit the characteristics of both viscous fluid and elastic solid [1]. What is even more complicated is to consider viscoelastic fluid dynamics in the presence of another fluid or another two kinds of fluids. Yet we cannot ignore this tough issue, as it is often the case in important fields such as food processes [2], blood flows [3,4], and more specifically, in reservoir engineering. Take the enhanced oil recovery (EOR) by polymer flooding as an example; it requires careful considerations of at least three phases such as oil, water, and polymer [5], and the incorporation of polymer viscoelasticity is a necessity [6–8].

For direct simulations of the ordinary three-phase Newtonian fluid flows, there have been several approaches available already, such as the front-tracking method [9,10], the level-set method [11–13], and the phase-field method [14–17]. Meanwhile, the mesoscopic lattice Boltzmann method (LBM) has gained much success in studying two-phase flows incorporated with other complexities [18–23]. More recently, a few LB models for ternary fluids came up [24–27]. The Rothman-Keller (RK) model [28–30] was straightforwardly extended to systems including three or more phases through adding evolution equations of the same form by Leclaire *et al.* [25]. The accuracy of their model was further improved for problems encountered with large density and viscosity ratios [31–33]. A three-component Shan-Chen model was also developed by applying three sets of LB equations (LBEs) interacting with each other [24]. Additionally, Liang *et al.* [26] and Sempere *et al.* [27] proposed three-phase models based on the phase-field theory almost at the same time.

As for LB models to account for the viscoelastic non-Newtonian effects, various strategies were applied covering both single-phase flows and two-phase flows [34]. By adding nonpropagating populations to the standard velocity models,

Giraud *et al.* [35] split the viscous stress tensor to consider the memory effects in Jeffreys viscoelastic fluids. Later this model was extended to three dimensions [36], and further two-phase free-energy-based models were carried out by Wagner *et al.* [37,38]. Dellar [39] also made improvements on the single-phase LB models for Jeffreys fluids by introducing an abstract tensor, which simplified the derivation. Additional sets of LBEs to recover constitutive equations were established for the upper-convected Maxwell (UCM) fluids [40] and for the Oldroyd-B fluids [41,42], respectively. Yet these kinds of models are less efficient, especially for two-phase extensions [43], since evolutions for three sets of LBEs are necessary. Another group of approaches were achieved by adding a forcing term to the momentum LBE. For the Oldroyd-B fluids, Su *et al.* [44] derived a very complicated term, while for the Maxwell fluids it was much simpler, as presented by Ispolatov and Grant [45]. Yoshino *et al.* [46] further extended Ispolatov and Grant's model to two-phase flows in the framework of a free-energy model [47]. However, these Maxwell LB models did not recover the momentum equation for real Maxwell fluids, as we discuss in the following sections.

Nevertheless, three-phase models for viscoelastic fluid flows are still rare. In this paper, we are to establish such a LB framework combining the RK-type three-phase model and the Maxwell viscoelastic constitutive equation. In Sec. II, the basic three-phase Newtonian fluid model and its extension to viscoelastic fluids are introduced, with the implementation of wetting boundaries on complex solid surfaces described in detail. In Sec. III, several benchmarks are presented both for the basic three-phase code and for the viscoelastic model. In Sec. IV, the present model is further applied to investigate the issue of dispersed polymer flooding in complex pore channels. Finally, conclusions are drawn in Sec. V.

**II. NUMERICAL METHODS****A. Three-phase LB scheme for Newtonian fluids**

We select the RK model in Leclaire *et al.*'s work [25] as our basic multiphase flow solver, along with a series of

\*Corresponding author: [mrwang@tsinghua.edu.cn](mailto:mrwang@tsinghua.edu.cn)

improvements on the multiple-relaxation-time (MRT) operator [33], the isotropic color gradient [31], and the momentum

correction [32]. The D2Q9 lattice is applied with the velocity vectors  $\mathbf{c}_i$  and the weight parameter  $W_i$ , defined as

$$\mathbf{c}_i = [c_{ix}, c_{iy}] = \begin{cases} [0, 0], & i = 0 \\ \{\cos[\frac{\pi}{2}(i-1)], \sin[\frac{\pi}{2}(i-1)]\}c, & i = 1, 2, 3, 4 \\ \{\cos[\frac{\pi}{4} + \frac{\pi}{2}(i-5)], \sin[\frac{\pi}{4} + \frac{\pi}{2}(i-5)]\}\sqrt{2}c, & i = 5, 6, 7, 8 \end{cases}, \quad (1)$$

$$W_i = \begin{cases} 4/9, & i = 0 \\ 1/9, & i = 1, 2, 3, 4 \\ 1/36, & i = 5, 6, 7, 8 \end{cases}. \quad (2)$$

In the RK-type LB model,  $N$  sets of distribution functions  $f_i^k$  denoting  $N$  kinds of fluids are introduced, corresponding to  $N$  sets of LB equations to capture the motion of each phase colored by  $k$ . The interaction between each phase is realized by additional collision operators. This idea is natural and simple, which makes the form of each LBE briefly kept the same as

$$\begin{aligned} f_i^k(\mathbf{x} + \mathbf{c}_i \Delta t, t + \Delta t) - f_i^k(\mathbf{x}, t) \\ = \Omega_i^k[f_i^k(\mathbf{x}, t)] + \Gamma_i \left( \frac{\rho^k}{\rho} \mathbf{F}(\mathbf{x}, t) \right), \end{aligned} \quad (3)$$

where  $\mathbf{x}$  is lattice position,  $\Delta t$  is the time step,  $\mathbf{c}_i$  is the lattice velocity with the discrete direction of  $i$ , and  $\Delta x = c \Delta t$  is the lattice spacing. The macroscopic phase density  $\rho^k$ , the total density  $\rho$ , and flow velocity  $\mathbf{u}$  are computed as follows:

$$\begin{aligned} \rho^k &= \sum_i f_i^k = \sum_i f_i^{k,eq}, \\ \rho &= \sum_k \rho^k, \quad \mathbf{u} = \left( \mathbf{F}/2 + \sum_i \sum_k f_i^k \mathbf{c}_i \right) / \rho. \end{aligned} \quad (4)$$

The modified forcing term  $\Gamma_i$  [48] is applied here to account for the total body force  $\mathbf{F}$  consisting of viscoelastic force  $\mathbf{F}_{el}$  and gravity  $\rho \mathbf{g}$ :

$$\begin{aligned} \Gamma_i \left( \frac{\rho^k}{\rho} \mathbf{F}(\mathbf{x}, t) \right) &= \frac{\rho^k}{\rho} \Delta t \left( 1 - \frac{1}{2\tau_{\text{eff}}} \right) \frac{3(\mathbf{c}_i - \mathbf{u}) \cdot \mathbf{F}}{c^2} \\ &\times W_i \left( \frac{3\mathbf{c}_i \cdot \mathbf{u}}{c^2} + \frac{9(\mathbf{c}_i \cdot \mathbf{u})^2}{2c^4} - \frac{3\mathbf{u}^2}{2c^2} \right) \end{aligned} \quad (5)$$

with the effective relaxation time  $\tau_{\text{eff}} = 0.5 + 3\nu_{\text{eff}}/(c^2 \Delta t)$ . The effective viscosity  $\nu_{\text{eff}}$  is the density-weighted interpolation of phase kinematic viscosity  $\nu^k$  as

$$\nu_{\text{eff}} = \sum_k \frac{\rho^k \nu^k}{\rho}. \quad (6)$$

Compared with the LBE for single-phase flow, the collision term  $\Omega_i^k$  in the RK model is combined by three sub operators:

$$\Omega_i^k = (\Omega_i^k)^M [(\Omega_i^k)^S + (\Omega_i^k)^I], \quad (7)$$

in which  $(\Omega_i^k)^S$  is the single-phase operator,  $(\Omega_i^k)^I$  is the perturbation operator (or interfacial operator), and  $(\Omega_i^k)^M$  is the recoloring operator (or mass conserving operator).

The MRT single-phase operator is in charge of the fluid momentum evolution, which is written as

$$\begin{aligned} (\Omega_i^k)^S &= f_i^k - (\mathbf{M}^{-1} \mathbf{K} \mathbf{M} [f_0^k - f_0^{k,eq}, f_1^k \\ &- f_1^{k,eq}, \dots, f_8^k - f_8^{k,eq}]^T)_i, \end{aligned} \quad (8)$$

where  $\mathbf{M}$  is the transformation matrix given in Appendix A and  $\mathbf{K}$  is the diagonal matrix of relaxation parameters [33]:

$$\begin{aligned} \mathbf{K} &= \text{diag} \left( \frac{4}{5\tau_{\text{eff}}}, \frac{4}{5\tau_{\text{eff}}}, \frac{4}{5\tau_{\text{eff}}}, \frac{4}{5\tau_{\text{eff}}}, \right. \\ &\left. \frac{1}{\tau_{\text{eff}}}, \frac{1}{\tau_{\text{eff}}}, \frac{4}{5\tau_{\text{eff}}}, \frac{4}{5\tau_{\text{eff}}}, \frac{4}{5\tau_{\text{eff}}} \right). \end{aligned} \quad (9)$$

The equilibrium distribution function  $f_i^{k,eq}$  is given by

$$\begin{aligned} f_i^{k,eq}(\rho^k, \mathbf{u}, \alpha^k) \\ = \rho^k \left( \phi_i^k + W_i \left( \frac{3\mathbf{c}_i \cdot \mathbf{u}}{c^2} + \frac{9(\mathbf{c}_i \cdot \mathbf{u})^2}{2c^4} - \frac{3\mathbf{u}^2}{2c^2} \right) \right) + \Phi_i^k \end{aligned} \quad (10)$$

with

$$\phi_i^k = \begin{cases} \alpha^k, & i = 0 \\ (1 - \alpha^k)/5, & i = 1, 2, 3, 4. \\ (1 - \alpha^k)/20, & i = 5, 6, 7, 8 \end{cases} \quad (11)$$

$\alpha^k$  ( $0 < \alpha^k < 1$ ) is the parameter which controls the density ratios between fluids  $k$  and  $l$  as

$$\frac{\rho^{k,0}}{\rho^{l,0}} = \frac{1 - \alpha^l}{1 - \alpha^k}, \quad (12)$$

where 0 indicates the initial setup of densities, and  $\alpha^* = 4/9$  is recommended for the least dense fluid [25].

In order to obtain the right momentum for various density ratios, the last term  $\Phi_i^k$  in Eq. (10) is necessarily introduced in [32] while was missed in [49]:

$$\Phi_i^k = \begin{cases} -3\nu_{\text{eff}}(\mathbf{u} \cdot \nabla \rho^k)/c^2, & i = 0 \\ 4\nu_{\text{eff}}(\mathbf{D}^k : \mathbf{c}_i \otimes \mathbf{c}_i)/c^4, & i = 1, 2, 3, 4, \\ \nu_{\text{eff}}(\mathbf{D}^k : \mathbf{c}_i \otimes \mathbf{c}_i)/c^4, & i = 5, 6, 7, 8 \end{cases} \quad (13)$$

with tensor  $\mathbf{D}^k = [(\mathbf{u} \otimes \nabla \rho^k) + (\mathbf{u} \otimes \nabla \rho^k)^T]/8$ .

The perturbation operator is in charge of the interfacial action for multiphase flow, which is written as

$$(\Omega_i^k)^I = f_i^k + \sum_{l(l \neq k)} \frac{A^{kl} C^{kl}}{2} |\mathbf{G}^{kl}| \left( W_l \frac{(\mathbf{c}_i \cdot \mathbf{G}^{kl})^2}{|\mathbf{c}_i|^2 |\mathbf{G}^{kl}|^2} - B_l \right) \Delta x, \quad (14)$$

where  $\mathbf{G}^{kl}$  is a ‘‘color’’ gradient perpendicular to the interface between phase  $k$  and  $l$ :

$$\mathbf{G}^{kl}(\mathbf{x}, t) = \frac{\rho^l}{\rho} \nabla \left( \frac{\rho^k}{\rho} \right) - \frac{\rho^k}{\rho} \nabla \left( \frac{\rho^l}{\rho} \right), \quad (15)$$

and

$$B_i = \begin{cases} -4/27, & i = 0 \\ 2/27, & i = 1, 2, 3, 4. \\ 5/108, & i = 5, 6, 7, 8 \end{cases} \quad (16)$$

$C^{kl} = \min\{10^6 \frac{\rho^k \rho^l}{\rho^{k,0} \rho^{l,0}}, 1\}$  is a concentration factor which limits the range of interfacial action suggested in [25]. Parameter  $A^{kl}$  is determined by the interfacial tension  $\gamma^{kl}$ :

$$A^{kl} = A^{lk} = \frac{9}{2} \frac{\gamma^{kl}}{\tau_{\text{eff}} c^2 \Delta x}. \quad (17)$$

Although the second operator successfully captures the interfacial dynamics, it will also cause the mixing of fluids and break the mass conservation for each phase. To overcome this and ensure perfect mass conservation, the recoloring operator is indispensable, which is as follows:

$$\begin{aligned} (\Omega_i^k)^M &= \frac{\rho^k}{\rho} \sum_k f_i^k + \sum_{l(l \neq k)} \left[ \beta^{kl} \frac{\rho^k \rho^l}{\rho^2} \cos(\varphi_i^{kl}) \right. \\ &\quad \left. \times \sum_k f_i^{k,eq}(\rho^k, 0, \alpha^k) \right], \end{aligned} \quad (18)$$

in which the parameter  $\beta^{kl}$  controls the thickness of the  $k$ - $l$  interface with a special relation with  $\beta^0$  ( $0 < \beta^0 \leq 1$ ) given in [25], and  $\varphi_i^{kl}$  is the angle between  $\mathbf{c}_i$  and  $\mathbf{G}^{kl}$ .

At this point, combining the above equations gives the basic LB scheme for multiphase Newtonian fluid flow with large density and viscosity ratios simultaneously. It is worth mentioning that there are some slight differences between Eqs. (13), (14), and (17) in this work and those in the original model due to dimension correction.

### B. Extension to viscoelastic fluids

In this section, the RK-type LB scheme is developed to deal with viscoelastic fluids. The widely applied Maxwell constitutive relation is introduced here to account for the accumulated stress and memory effect of viscoelastic polymer:

$$\dot{\boldsymbol{\epsilon}} = \frac{\boldsymbol{\sigma}}{\eta^p} + \frac{1}{E} \frac{d\boldsymbol{\sigma}}{dt}, \quad (19)$$

where  $\boldsymbol{\sigma}$  is the stress,  $\dot{\boldsymbol{\epsilon}}$  is the strain rate,  $E$  is the elastic modulus, and  $\eta^p$  is the intrinsic polymer dynamic viscosity. Since the stress has finite value at  $t = -\infty$ , it can be obtained by integrating Eq. (19) over time:

$$\boldsymbol{\sigma}(\mathbf{x}, t) = \frac{\eta^p}{\tau^{el}} \int_{-\infty}^t \exp\left(-\frac{t-t'}{\tau^{el}}\right) \dot{\boldsymbol{\epsilon}}(\mathbf{x}, t') dt', \quad (20)$$

with the memory time  $\tau^{el} = \eta^p/E$ .

Taking the divergence of the elastic stress deduces a body force

$$\mathbf{F}_{el}(\mathbf{x}, t) = \nabla \cdot \boldsymbol{\sigma} = \frac{\eta^p}{\tau^{el}} \int_{-\infty}^t \exp\left(-\frac{t-t'}{\tau^{el}}\right) \nabla^2 \mathbf{u}(\mathbf{x}, t') dt'. \quad (21)$$

Then by assuming

$$\Delta t \ll \tau^{el}, \quad \exp\left(-\frac{\Delta t}{\tau^{el}}\right) = 1 - \frac{\Delta t}{\tau^{el}}, \quad (22)$$

it can be easily discretized by time step as

$$\begin{aligned} \mathbf{F}_{el}(\mathbf{x}, t) &= \left(1 - \frac{\Delta t}{\tau^{el}}\right) \mathbf{F}_{el}(\mathbf{x}, t - \Delta t) \\ &\quad + \frac{\eta^p \Delta t}{\tau^{el}} \nabla^2 \mathbf{u}(\mathbf{x}, t - \Delta t). \end{aligned} \quad (23)$$

In the previous viscoelastic single-phase LB model [45] and a phase-field two-phase LB model [46], the above body force was directly added to the LBEs. However, in such a manner, the LBEs in the single-phase region cannot correctly return to the real momentum equation for Maxwell materials. This is due to the remaining excess ‘‘LB viscous term’’  $\eta_{\text{LB}} \nabla^2 \mathbf{u}$  in the momentum equation as

$$\partial_t \rho \mathbf{u} + (\mathbf{u} \cdot \nabla) \rho \mathbf{u} = -\nabla p + \eta_{\text{LB}} \nabla^2 \mathbf{u} + \mathbf{F}_{el} + \rho \mathbf{g}, \quad (24)$$

where  $p$  is the pressure and  $\eta_{\text{LB}}$  is the dynamic viscosity originated from the ordinary LBE for Newtonian fluids. Using the integration by parts, another equivalent form of Eq. (21) is derived as given in Appendix B, where the term  $\eta^p \nabla^2 \mathbf{u}(\mathbf{x}, t)$  should be regarded as the viscous term instead of  $\eta_{\text{LB}} \nabla^2 \mathbf{u}$  in the normal LB framework. Unfortunately, the last term in Eq. (A2) cannot be stably computed although using the same discretization method for Eq. (21).

Therefore, Eq. (23) is still applied in this work, but unlike the previous ones in Refs. [45] and [46],  $\eta_{\text{LB}}$  values are set to zero for all Maxwell fluids. As a result, the real momentum equation for Maxwell fluids in the single-phase region is recovered as

$$\partial_t \rho \mathbf{u} + (\mathbf{u} \cdot \nabla) \rho \mathbf{u} = -\nabla p + \mathbf{F}_{el} + \rho \mathbf{g}. \quad (25)$$

Finally, by substituting Eq. (23) into Eqs. (4) and (5), and by setting  $\eta_{\text{LB}} = 0$ , we obtain the present RK-type multiphase model for viscoelastic fluids with large density and viscosity ratios. The derivatives then in Eqs. (13), (15), and (23) are evaluated through a fourth-order gradient operator by [50], which greatly improves the numerical accuracy [31].

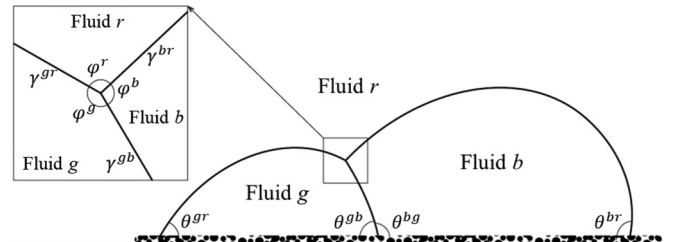


FIG. 1. Sketch of a three-phase system on solid walls, with  $r$ ,  $g$ ,  $b$  representing red, green, and blue fluids.

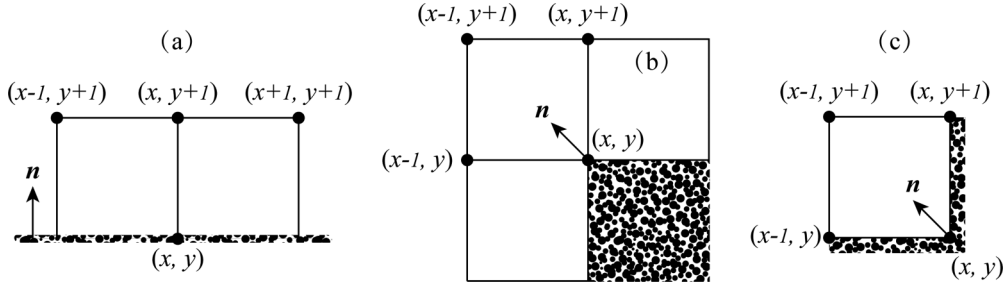


FIG. 2. Three typical wall boundary configurations for concentrations: (a) flat case, (b) corner case 1, and (c) corner case 2.

### C. Implementation of the wetting boundary condition

In order to be applicable to porous media, fluid-solid interaction is essential and wetting boundary conditions should be implemented. The evolving contact angle in two-phase RK models was originally achieved by directly setting virtual wall densities which interact with the neighboring fluid densities through the “color” gradient [51]. While inspired by the work on diffuse-interface theory [17,52], virtual concentrations  $C^k = \rho^k/\rho$  are also introduced on solid lattices for the three-phase model here. In this method, the concentrations as well as densities on solid sites are updated at every time step, which will lead to better wetting dynamics over that in Ref. [51]. The following equations determine the virtual concentrations:

$$-\mathbf{n} \cdot \nabla C^k = \tan\left(\frac{\pi}{2} - \theta^k\right) |\nabla C^k - (\mathbf{n} \cdot \nabla C^k) \mathbf{n}|, \quad (26)$$

$$C^k|_{x,y} = \begin{cases} C^k|_{x,y+1} + \frac{1}{2} \tan\left(\frac{\pi}{2} - \theta^k\right) |C^k|_{x+1,y+1} - C^k|_{x-1,y+1}|, & \text{case (a)} \\ C^k|_{x-1,y+1} + \tan\left(\frac{\pi}{2} - \theta^k\right) |C^k|_{x,y+1} - C^k|_{x-1,y}|, & \text{case (b and c)} \end{cases}. \quad (29)$$

Similarly, by considering other possible orientations of  $\mathbf{n}$  in a porous media, the wetting boundary conditions are fully implemented. Actually, this idea has been nicely applied to a RK model for flat surfaces by Jiang and Tsuji [49] very recently, yet simple complete wetting conditions were still used for complex geometries.

## III. BENCHMARKS

Before the discussions on viscoelastic polymer flooding in porous media, a series of benchmarks are performed.

### A. Multilayer Couette flow

In the first case, we consider a 2D multilayer Couette flow to verify the accuracy of the basic Newtonian code for multiphase momentum calculation. As shown in Fig. 3, four layers of fluids are placed parallel between two infinite plates with the width of each layer  $h = 3$  mm. The system consists of red fluid ( $\rho^r = 1000$  kg/m<sup>3</sup>,  $\nu^r = 1 \times 10^{-6}$  m<sup>2</sup>/s), green fluid ( $\rho^g = 100$  kg/m<sup>3</sup>,  $\nu^g = 5 \times 10^{-6}$  m<sup>2</sup>/s), and blue fluid ( $\rho^b = 350$  kg/m<sup>3</sup>,  $\nu^b = 9 \times 10^{-6}$  m<sup>2</sup>/s), all driven by the upper plate with a wall velocity  $u_w = 0.01$  m/s. Given these values, the theoretical results for the cross-sectional

where for a two-phase system ( $k$ - $l$  phase)

$$\theta^k = \theta^{kl} = \pi - \theta^{kl}, \quad (27)$$

and for a three-phase system ( $r$ - $g$ - $b$  phase) sketched in Fig. 1,

$$\theta^r = \frac{C^b}{1 - C^r} \theta^{rb} + \frac{C^g}{1 - C^r} \theta^{rg}, \quad (28a)$$

$$\theta^g = \frac{C^b}{1 - C^g} \theta^{gb} + \frac{C^r}{1 - C^g} \theta^{gr}, \quad (28b)$$

$$C^b = 1 - C^r - C^g. \quad (28c)$$

A finite difference scheme is used to discretize Eq. (26), which will lead to different expressions for various wall configurations. Taking three typical configurations shown in Fig. 2, for example,  $C^k|_{x,y}$  on solid nodes ( $x, y$ ) are calculated accordingly:

momentum distribution at the steady state can be calculated according to Ref. [25].

In our simulation, the fluid domain covers  $10 \times 122$  lattices. Periodic boundary conditions are applied on the left and right, bounce-back rule is applied on the lower stationary wall, while a moving boundary condition is adopted [53,54] for the upper wall. Other parameters, such as interface tensions and lattice velocity, are set as  $\gamma = 0.01$  N/m and  $c = 1$  m/s, respectively.

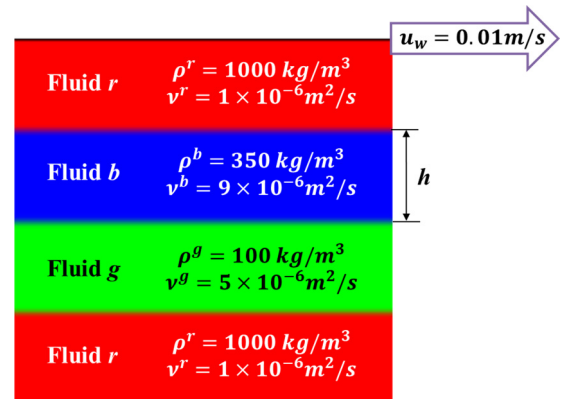


FIG. 3. Sketch of a multilayer Couette flow.

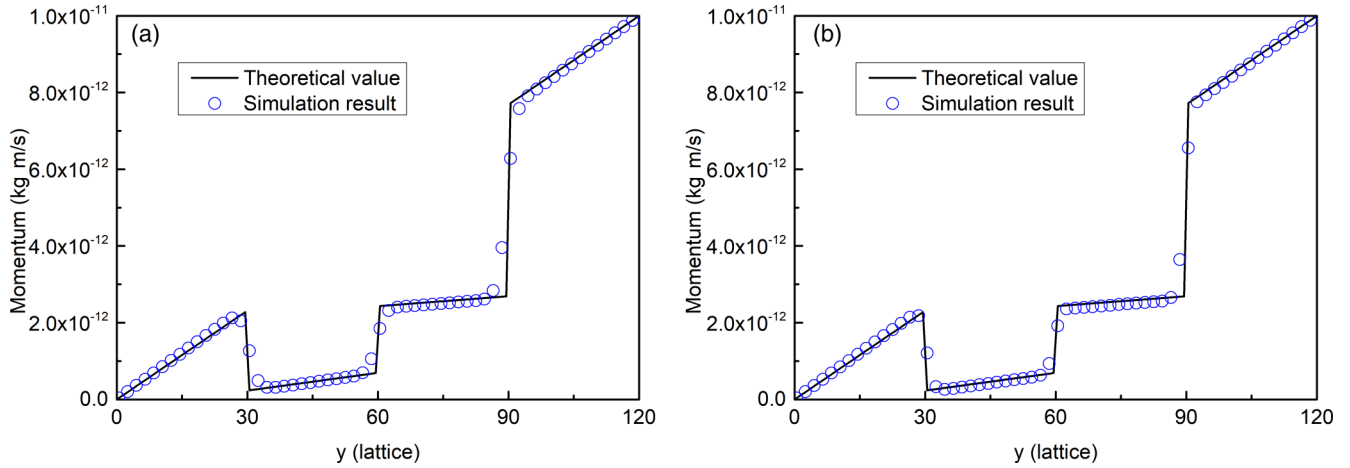


FIG. 4. Momentum validations for the multilayer Couette flow with (a)  $\beta^0 = 0.6$  and (b)  $\beta^0 = 0.85$ .

Here we test two different values of  $\beta^0$ : one is 0.6 for the rougher interface and the other is 0.85 for the sharper interface. The steady-state momentum results are obtained in Fig. 4, and both of them match well with the theoretical profile. These results indicate that the multiphase hydrodynamics can be correctly captured by this model, and the choice of  $\beta^0$  has little impact on the fluid momentum.

### B. Three-phase wettability

The goal of this case is to examine whether or not the implementation of wetting boundary conditions can describe the static contact angles of three-phase fluids in contact with solid. The three-phase system in Fig. 1 is considered. Initially, two symmetrical quarter-circular droplets (green and blue fluids with initial radius  $R_0 = 2.5$  mm) are placed closely in contact with each other on the bottom wall, surrounded by the bulk red fluid. Densities and viscosities of these fluids are  $\rho^r = 1000$  kg/m<sup>3</sup>,  $\nu^r = 1 \times 10^{-4}$  m<sup>2</sup>/s,  $\rho^g = 200$  kg/m<sup>3</sup>,  $\nu^g = 1 \times 10^{-4}$  m<sup>2</sup>/s,  $\rho^b = 800$  kg/m<sup>3</sup>, and  $\nu^b = 1 \times 10^{-4}$  m<sup>2</sup>/s. When given certain interface tensions ( $\gamma^{gr}$ ,  $\gamma^{gb}$ , and  $\gamma^{br}$ ) and any two contact angles (e.g.,  $\theta^{gr}$  and  $\theta^{br}$ ), the system will relax to its equilibrium state, with the remaining contact angle ( $\theta^{gb}$ ) being determined by the following correlation [27]:

$$\gamma^{rg} \cos \theta^{rg} + \gamma^{gb} \cos \theta^{gb} + \gamma^{br} \cos \theta^{br} = 0. \quad (30)$$

And also, the phase angles ( $\varphi^r$ ,  $\varphi^g$ , and  $\varphi^b$ ) are determined through

$$\frac{\sin \varphi^r}{\gamma^{gb}} = \frac{\sin \varphi^g}{\gamma^{br}} = \frac{\sin \varphi^b}{\gamma^{rg}}. \quad (31)$$

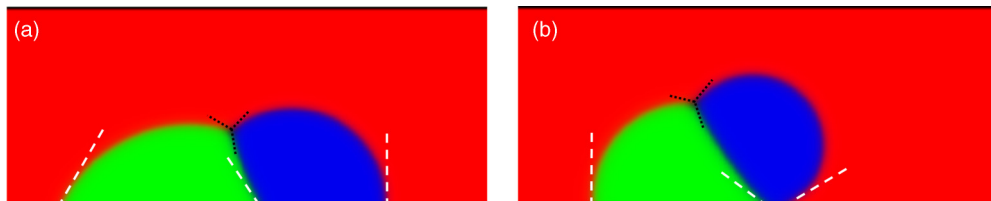


FIG. 5. Validation results of the three-phase wettability with (a)  $\theta^{gr} = 60^\circ$ ,  $\theta^{br} = 90^\circ$ ,  $\theta^{gb} = 60^\circ$  and (b)  $\theta^{gr} = 90^\circ$ ,  $\theta^{br} = 150^\circ$ ,  $\theta^{gb} = 30^\circ$ .

We present two groups of simulations in this work. Contact angles of  $\theta^{gr} = 60^\circ$ ,  $\theta^{br} = 90^\circ$ ,  $\theta^{gb} = 60^\circ$  and  $\theta^{gr} = 90^\circ$ ,  $\theta^{br} = 150^\circ$ ,  $\theta^{gb} = 30^\circ$  are imposed on group (a) and group (b), respectively. The interface tensions are all set as  $\gamma = 0.01$  N/m. The simulation domains are divided into  $100 \times 42$  lattices, with periodic boundaries on left and right and solid walls on top and bottom. The lattice spacing  $\Delta x = 0.1$  mm, lattice velocity  $c = 1$  m/s, and  $\beta^0 = 0.65$  are assigned. Then we export the phase distributions at time step  $t = 15000\Delta t$  when equilibrium states establish, as shown in Fig. 5. It is observed that the evolved contact angles in our simulations agree quite well with the prescribed values. Note that the phase angles ( $\varphi^r$ ,  $\varphi^g$ , and  $\varphi^b$ ) are all around  $120^\circ$ , which is also coincident with theoretical values when interface tensions are identically imposed. Therefore, the implemented three-phase wetting boundary condition is confirmed.

### C. Validation of viscoelastic extension

With the above two cases as benchmarks for the basic multiphase Newtonian model, this section draws attention to the validation of its extension to viscoelastic fluids. Indeed, there is no rigorous benchmark for three-phase viscoelastic fluid flow, and even for the simple two-phase case. However, the qualitative benchmark for the problem of a Newtonian bubble rising in a viscoelastic fluid should be possible. The schematic of this problem is illustrated in Fig. 6, where a Newtonian bubble (fluid  $b$ ) with initial radius of  $R$  is freely released in the bulk viscoelastic fluid ( $r$ ). Then driven by the buoyancy force due to gravitational acceleration  $\mathbf{g}$ , the bubble will rise in the closed tank. Under certain conditions of relatively large capillary number (Ca) and Deborah number

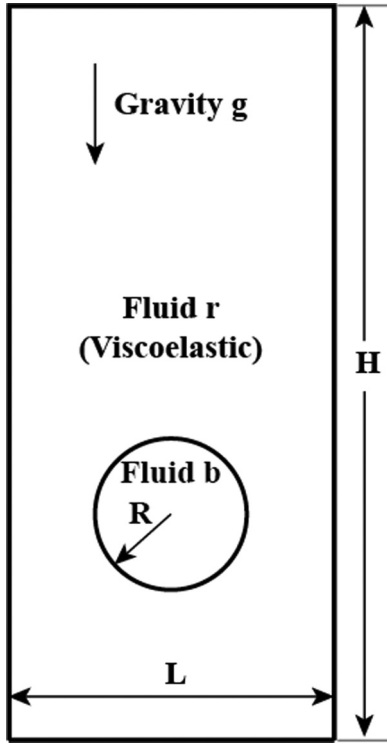


FIG. 6. Physical model of a Newtonian bubble (fluid b) rising in a viscoelastic fluid (r).

(De), the bubble will become a “cusp shape” with a sharp tip at the tail, and a “negative wake” behind the bubble was often reported [55–60]. These phenomenon feature the viscoelastic behavior of bulk fluid, and the reasons were nicely summarized recently in Ref. [61]: Due to the viscoelastic memory effect, elastic normal stresses will form against the upstream buoyancy force, which leads to the tip formation; to some extent, velocities behind the bubble will detach, thus a “negative wake” appears; then this “negative wake” will yield downstream shear stresses, which further favors the tip elongation.

We perform two sets of simulations to compare the bubble rising dynamics in a viscoelastic fluid and in a Newtonian fluid. All closed wall boundaries with completely bulk fluid wet conditions are applied in these simulations. In these simulations, the parameters are set as follows. The tanks with size of  $L \times H = 20 \text{ mm} \times 40 \text{ mm}$  are covered by  $201 \times 401$  lattices using lattice spacing  $\Delta x = 0.1 \text{ mm}$  and time step  $\Delta t = 1.25 \times 10^{-6} \text{ s}$ . Initial radius of the Newtonian bubbles are  $R = 3 \text{ mm}$ . Bubble densities  $\rho^b = 100 \text{ kg/m}^3$ , dynamic viscosity  $\eta^b = 0.015 \text{ Pa s}$ , bulk fluid densities  $\rho^r = 1000 \text{ kg/m}^3$ , gravitational acceleration  $g = 9.8 \text{ m/s}^2$ , interface tensions  $\gamma = 0.01 \text{ N/m}$ , and interface width parameters  $\beta^0 = 0.8$  are used in both simulations. For the viscoelastic fluid, the memory time is set as  $\tau^{el} = 0.1 \text{ s}$ , and the intrinsic polymer viscosity in Eq. (19) is set as  $\eta^p = 0.875 \text{ Pa s}$ , while for the bulk referential Newtonian fluid, its phase dynamic viscosity is set equal to  $\eta^p$  as  $\eta^r = 0.875 \text{ Pa s}$ . Thereafter, defining the characteristic length  $L^* = 2R$  and velocity  $V^* = \sqrt{2gR}$ , the capillary number and the Deborah number are calculated as  $\text{Ca} = \eta^p V^* / \gamma = 2.12$  and  $\text{De} = V^* \tau^{el} / L = 4.04$ , respectively.

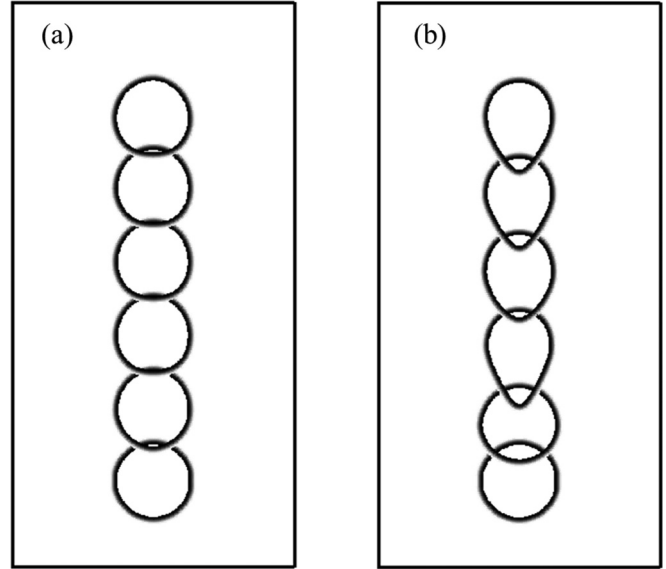


FIG. 7. Comparisons of the bubble rising processes (a) in a Newtonian fluid and (b) in a viscoelastic fluid.

Our results are presented in Fig. 7 and Figs. 8(a) and 8(b). As is seen, notable differences are found between the viscoelastic case and the Newtonian case. Figure 7 compares the shape evolution of the rising bubbles, and the “cusp shape” is only observed for the viscoelastic case. In the streamline comparison in Fig. 8, a “negative wake” and two vortex rings are captured behind the bubble in the viscoelastic fluid, while they are not found in the Newtonian fluid. Since these two major viscoelastic features are well recovered in the above simulations, the capabilities of our extended model to describe the flow of multiphase viscoelastic fluids are validated.

Note that the assumption of Eq. (22) is important when viscoelastic behavior needs to be considered. Therefore in order to present a common criterion for  $\Delta t$ , effects of the calculation time step are further discussed in Figs. 8(b)–8(d). These figures are all captured at the same physical time of  $t = 0.105 \text{ s}$ . It is observed that although increasing  $\Delta t$  does not affect the bubble shape and the characteristic of “negative wake” qualitatively, it will lead to unstable streamlines numerically. Then we quantitatively compare the cross-sectional vertical velocity profiles extracted through the center of two vortexes beside the bubble as shown in Fig. 9. The velocity profiles indicate that the instability decreases with the decreasing of time step, which is in accordance with the assumption. The smooth results are obtained when the nondimensional time step  $\Delta t^* = \Delta t / \tau^{el}$  drops to  $1.25 \times 10^{-5}$ . As a consequence, we recommend a criterion for the time step in this model as  $\Delta t < 1.25 \times 10^{-5} \tau^{el}$ . Meanwhile, a very small value of  $\Delta t$  is usually not expected, since it will drastically increase the simulation cost. Also shown in Fig. 9 is the errors introduced by the excess LB viscosity  $\eta_{LB}$ , which prove our theoretical derivation and indicate again the necessary of removal of the excess viscous term by the present model. As depicted, the maximum velocity values drop 7.1% and 13%, respectively, by adding  $\eta_{LB}$  with only 1.14% and 2.28% magnitudes of the polymer viscosity. Even more serious errors occur when  $\eta_{LB}$

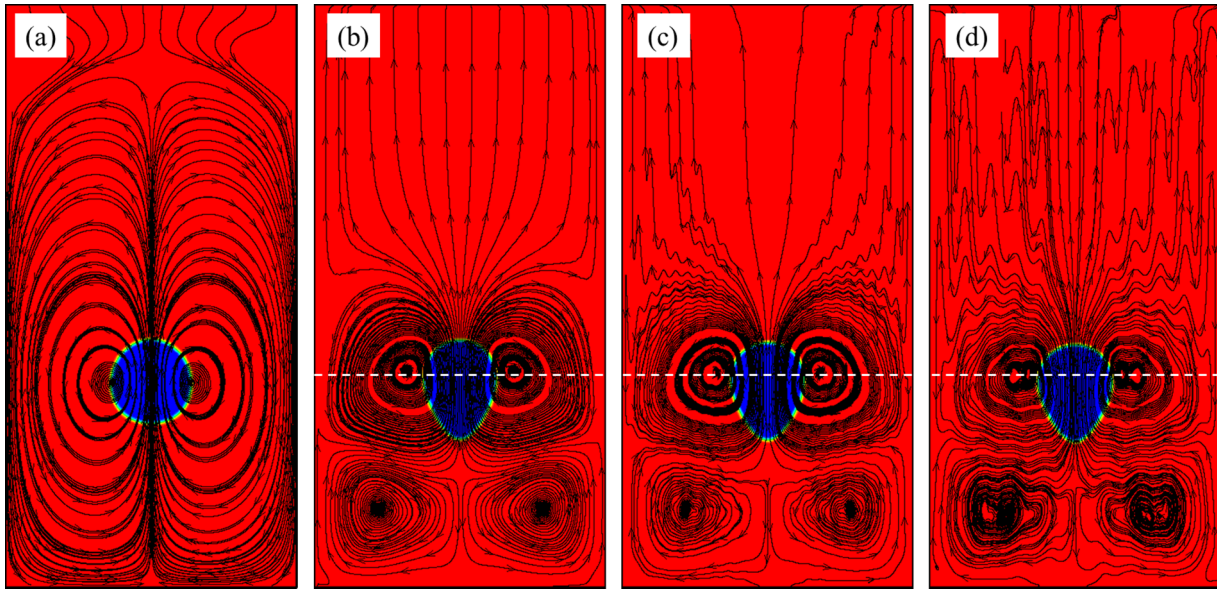


FIG. 8. Comparisons of the streamlines during bubble rising (a) in a Newtonian fluid and (b)–(d) in a viscoelastic fluid. In (c) and (d), the time steps used for calculations are changed to  $\Delta t = 2.5 \times 10^{-6}$  s and  $\Delta t = 5 \times 10^{-6}$  s, respectively.

increases to  $11.4\% \eta^p$ , and the “negative wake” is no longer captured, as shown in the subplot of Fig. 9.

IV. RESULTS AND DISCUSSION

In this section, displacement of oil by the dispersed polymer gel system is further investigated, with focus on the effects of polymer’s viscous and elastic properties. The schematic of our simulation setup and the initial configuration of fluids are shown in Fig. 10(a), with red representing oil, blue representing water, green representing the viscoelastic polymer, and black being the solid rock. The main porous region is constructed by two crossed channels with a notable difference in width, which is inspired by the supposed sketch in Ref. [62] to illustrate the

blocking and diverting mechanisms. In order to generate the dispersed polymers, the idea from microfluidic fields [63] is introduced, where we construct a “polymer generation device.” In this device, polymers enter from the left pipe with area flow rate  $Q_p$ , which will be cut into discontinuous drops by the water on two sides with flow rate  $Q_w$ . In addition, a buffer is attached to the right side of the main region to minimize the possible outlet effects.

The calculation domain contains  $650 \times 152$  lattices in total, with  $463 \times 152$  lattices covering the main porous region and  $38 \times 152$  lattices covering the outlet buffer. Three inlet pipes are set with the same width of 20 lattices. Lattice spacing  $\Delta x = 0.5 \mu\text{m}$  and time step  $\Delta t = 1.111 \times 10^{-9}$  s are used. Constant flow rate boundary conditions are applied to three inlets using the nonequilibrium extrapolation method [64], while the convective outflow boundary condition [65] is used at the outlet. For solid-fluid interactions, the prescribed wetting boundaries are adopted with contact angles set as  $\theta^{wo} = 90^\circ$ ,  $\theta^{pw} = 160^\circ$ , and  $\theta^{op} = 20^\circ$ . Other physical parameters like the densities are  $\rho^w = 1000 \text{ kg/m}^3$ ,  $\rho^o = 800 \text{ kg/m}^3$ , and  $\rho^p = 900 \text{ kg/m}^3$ ; the water and oil dynamic viscosities are  $\eta^w = 0.001 \text{ Pa s}$  and  $\eta^o = 0.02 \text{ Pa s}$ ; the flow rates are  $Q_p = 1.5 \times 10^{-6} \text{ m}^2/\text{s}$  and  $Q_w = 2 \times 10^{-6} \text{ m}^2/\text{s}$ ; the interface tensions are  $\gamma^{wo} = 0.012 \text{ N/m}$ ,  $\gamma^{pw} = 0.01 \text{ N/m}$ , and  $\gamma^{op} = 0.01 \text{ N/m}$ ; and the default viscoelastic properties of polymer are set as  $\eta^p = 0.05 \text{ Pa s}$  and  $E = 5000 \text{ Pa}$ .

Primarily, we compared the dispersed polymer flooding with pure water flooding in which the left inlet is changed to water injection but the same flow rate is kept. The displacing processes are presented in Fig. 11, where the cumulative injection volume of fluids is normalized by the pore volume (PV) of the main porous region. As is seen for the referential water flooding case in Fig. 11(a), the oil in large channels is quickly displaced, while there is no water entering into the small channels until 1PV injection. As long as the fast displacement in large channels happens, a main flow path will

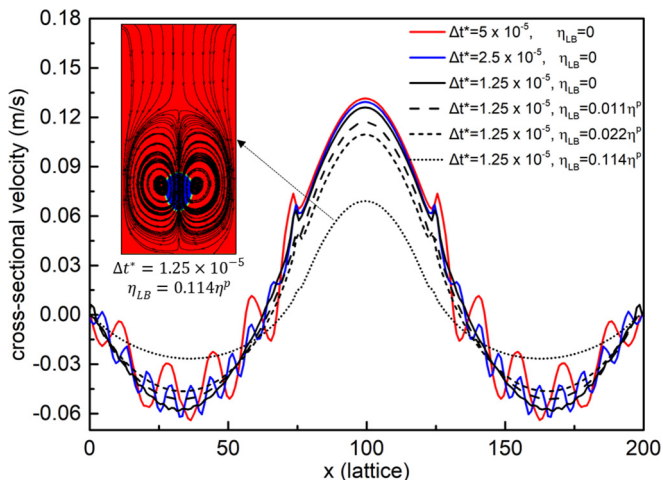


FIG. 9. Effects of time step and the excess LB viscosity  $\eta_{LB}$  on the present model, where the cross-sectional velocities are extracted through the white dash lines shown in Fig. 8, and the nondimensional time step  $\Delta t^* = \Delta t / \tau^{cl}$  is used.

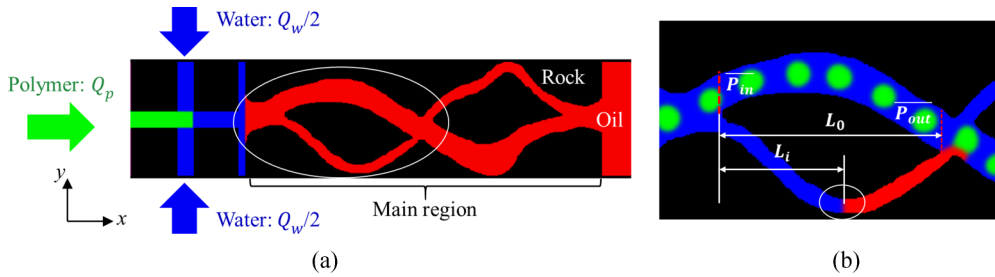


FIG. 10. (a) Initial setup for the simulation of oil displacement by the dispersed polymer system. (b) An enlarged view of the first cross for illustrations of the nondimensional displacing front position in the lower channel and mean pressures in the upper channel.

be formed and lead to the most water continuously following this path. However, on the other hand, almost no water will sweep into the small channels, and the weak flow there may even be cut and trapped by the main flow. Such poor displacing conditions are well overcome by introducing the dispersed polymers as shown in Fig. 11(b). These polymers are also preferentially travel through the large channels, yet the main flow is significantly suppressed compared with water flooding due to their higher viscous property. The blocking in large channels will help divert more water to penetrate into the small channels, thus recovering more trapped oil and providing much better sweep efficiency. Moreover, the pushing and dragging effects of polymers are observed, which further benefits the oil recovery.

Thereafter, impacts of the intrinsic polymer viscosity  $\eta^p$  and the elastic modulus  $E$  are discussed. In order to present more quantitative comparisons, a nondimensional displacing front position in the first lower small channel is introduced, as illustrated in Fig. 10(b). It is defined as the penetration length of water  $L_i$  in  $x$  direction divided by the total first cross length  $L_0$ . For the present crossed structure, evolution speed of this front position reflects the sweep efficiency and enhanced oil recovery (EOR) capability of the polymers. Figure 12(a) gives the effect of polymer viscosity  $\eta^p$  on the front evolution, as

faster evolution is found for higher viscosity case. The result indicates the monotonous increase of sweep efficiency with polymer viscosity, which is in accordance with the traditional polymer flooding results. On the one hand, higher viscosity represents more favorable condition with lower mobility ratio, but on the other hand, the viscous resistance in large channels increases with polymer viscosity and therefore more water is diverted into the small channels.

In Fig. 12(b), a similar trend is found for the effect of the polymer elastic modulus. To give further explanations, we count the mean pressure drop through the upper large channel in the first cross as described in Fig. 10(b). Comparisons of the pressure drop evolutions are shown in Fig. 13(a), where large fluctuations are found. Therefore clearer comparisons are presented by averaging the pressure drops from 1PV injection, as Fig. 13(b) gives the relation between the average upper pressure difference and polymer elastic modulus. Generally concluded from Fig. 13, the pressure drops required are higher for larger elastic modulus cases, which means that the resistance in large channels increases with the elastic modulus and consequently enhances the diversion capability. Deeper reasons should be explained by the relation between polymer particle deformability and its elastic modulus: as a smaller elastic modulus means lower stiffness, the polymers are easier to deform to adapt to the flow field, reducing the flow resistance. Therefore increasing the polymer elastic modulus also enhances oil recovery.

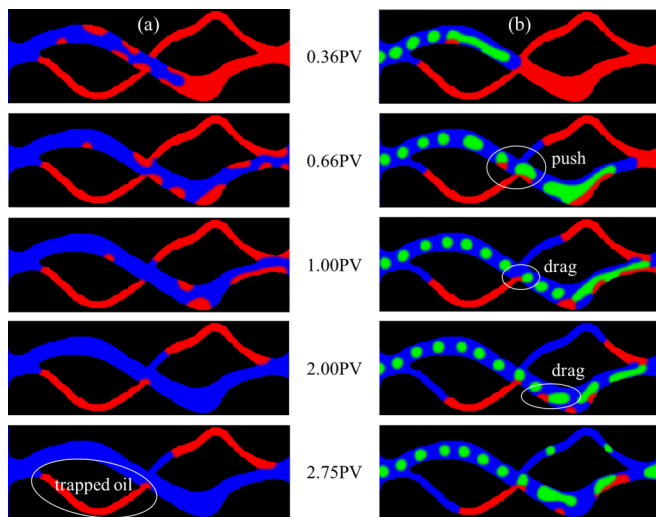


FIG. 11. Comparisons of oil displacement processes by (a) water and by (b) the dispersed polymer system. To record the displacing time, cumulative injection volume of fluids normalized by the pore volume (PV) of the main porous region is used.

V. CONCLUSION

In this paper, a three-phase lattice Boltzmann scheme for viscoelastic fluids is established. A RK-type multiphase LB model is set as the fundamental three-phase flow solver, which can deal with large-density-ratio cases. The viscoelastic effects are implemented by applying the Maxwell constitutive equation. The present approach modifies the previous single-phase and two-phase LB models for Maxwell viscoelastic fluid flows, by not only adding a forcing term but also removing the normal viscous term. Our derivations indicate that the correct Maxwell fluid momentum equation is successfully recovered by this modified method. In order to consider porous media applications, the algorithm for wetting boundary conditions on complex solid surfaces is described in detail. Thereafter, three typical benchmark cases are presented. Good agreements are found between the simulation results by the basic three-phase LB code and the corresponding theoretical solutions. Through the bubble rising tests, two distinguished viscoelastic behaviors

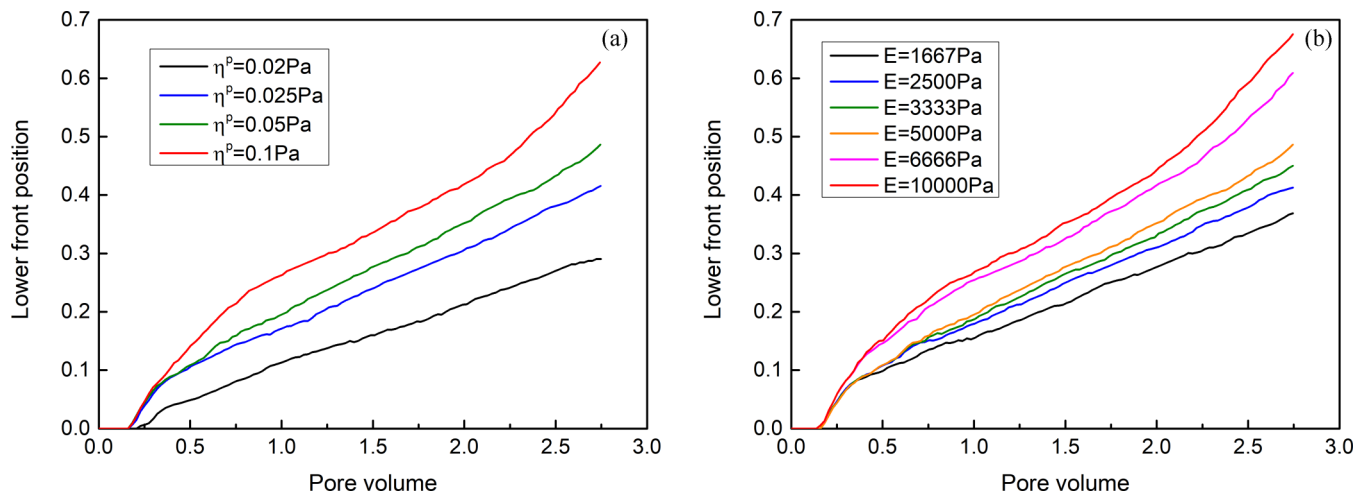


FIG. 12. Evolutions of the lower displacing front position with pore volume injected: (a) effect of  $\eta^p$  and (b) effect of  $E$ .

are observed which demonstrate that the present scheme for multiphase viscoelastic fluids is effective. In addition, the results further validate the necessity of removing the excess viscous term.

Finally, by applying the present LB framework, we are able to investigate the oil displacement processes by the dispersed viscoelastic polymer system. The effects of polymer intrinsic viscosity and its elastic modulus are separately discussed in a complex geometry with crossed channels. Our results show that the blocking and diverting capabilities of polymer enhance either with the increasing of polymer intrinsic viscosity or the increasing of elastic modulus, since the viscous resistance and the deformation resistance are increased, respectively. Future work on 3D extension is expected as well as applications to more complex rock geometries.

**ACKNOWLEDGMENTS**

This work is financially supported by the National Science Foundation of China (Grants No. 91634107 and No. U1562217) and the National Science and Technology

Major Project on Oil and Gas (Grant No. 2017ZX05013001). We gratefully thank Dr. S. Leclaire for discussions on the three-phase model, Dr. X. Wu on polymer EOR, and Mr. Y. Guo on the Maxwell constitutive equation.

**APPENDIX A: THE TRANSFORMATION MATRIX**

$$\mathbf{M} = \begin{bmatrix} 1 & 1 & 1 & 1 & 1 & 1 & 1 & 1 & 1 \\ 0 & 1 & 0 & -1 & 0 & 1 & -1 & -1 & 1 \\ 0 & 0 & 1 & 0 & -1 & 1 & 1 & -1 & -1 \\ -4 & -1 & -1 & -1 & -1 & 2 & 2 & 2 & 2 \\ 0 & 1 & -1 & 1 & -1 & 0 & 0 & 0 & 0 \\ 0 & 0 & 0 & 0 & 0 & 1 & -1 & 1 & -1 \\ 0 & 0 & 2 & 0 & -2 & -1 & -1 & 1 & 1 \\ 0 & 2 & 0 & -2 & 0 & -1 & 1 & 1 & -1 \\ 4 & -2 & -2 & -2 & -2 & 1 & 1 & 1 & 1 \end{bmatrix}. \tag{A1}$$

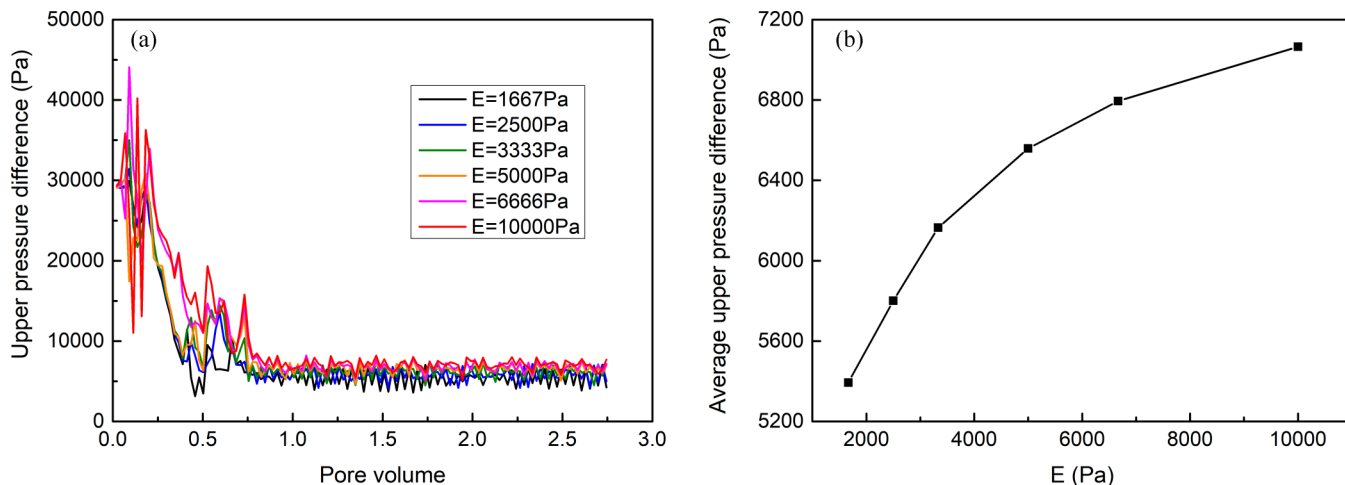


FIG. 13. (a) Evolutions of the upper channel pressure difference with pore volume injected. (b) Relation between the average upper channel pressure difference and polymer elastic modulus.

## APPENDIX B: ANOTHER EQUIVALENT FORM OF THE VISCOELASTIC FORCING TERM

Here we present another equivalent form of Eq. (21), as the viscoelastic forcing term can be expressed as follows as well by using the integration by parts:

$$F_{el}(\mathbf{x}, t) = \eta^p \nabla^2 \mathbf{u}(\mathbf{x}, t) - \eta_p \int_{-\infty}^t \exp\left(-\frac{t-t'}{\tau^{el}}\right) \left(\frac{\partial \nabla^2 \mathbf{u}(\mathbf{x}, t')}{\partial t'}\right) dt'. \quad (\text{B1})$$

Based on this expression, a polymer viscous term  $\eta^p \nabla^2 \mathbf{u}(\mathbf{x}, t)$  is extracted, which should have replaced the original viscous term  $\eta_{LB} \nabla^2 \mathbf{u}$  in the normal LB framework. Unfortunately, the last term in Eq. (A2) cannot be stably computed, although using the same discretization method as for Eq. (21). Therefore Eq. (23) is still applied in this work, but  $\eta_{LB}$  is set to zero to recover the correct momentum equation [Eq. (25)] for Maxwell fluids.

- 
- [1] M. M. Denn, *Annu. Rev. Fluid Mech.* **22**, 13 (1990).
- [2] M. A. Rao, in *Rheology of Fluid and Semisolid Foods: Principles and Applications*, edited by G. V. Barbosa-Canovas (Springer US, Boston, MA, 2007), p. 153.
- [3] M. Brust, C. Schaefer, R. Doerr, L. Pan, M. Garcia, P. E. Arratia, and C. Wagner, *Phys. Rev. Lett.* **110**, 078305 (2013).
- [4] N. Bessonov, A. Sequeira, S. Simakov, Y. Vassilevskii, and V. Volpert, *Math. Modell. Nat. Phenom.* **11**, 1 (2016).
- [5] C. Xie, W. Lv, and M. Wang, *J. Pet. Sci. Eng.* **161**, 683 (2018).
- [6] D. Wang, J. Cheng, Q. Yang, G. Wenchao, L. Qun, and F. Chen, in *SPE Annual Technical Conference and Exhibition* (Society of Petroleum Engineers, Dallas, TX, 2000).
- [7] M. Abdulbaki, C. Huh, K. Sepehrnoori, M. Delshad, and A. Varavei, *J. Pet. Sci. Eng.* **122**, 741 (2014).
- [8] H. R. Saghafi, A. Naderifar, S. Gerami, and M. A. Emadi, *Can. J. Chem. Eng.* **94**, 1880 (2016).
- [9] Z. Y. Luo, L. He, and B. F. Bai, *J. Fluid Mech.* **775**, 77 (2015).
- [10] Z. Y. Luo and B. F. Bai, *Phys. Fluids* **28**, 101901 (2016).
- [11] K. A. Smith, F. J. Solis, and D. Chopp, *Interfaces and Free Boundaries* **4**, 263 (2002).
- [12] R. I. Saye and J. A. Sethian, *Proc. Natl. Acad. Sci.* **108**, 19498 (2011).
- [13] J. O. Helland and E. Jettestuen, *Water Resour. Res.* **52**, 5376 (2016).
- [14] J. S. Kim and J. Lowengrub, *Interface. Free Bound.* **7**, 435 (2005).
- [15] F. Boyer and C. Lapuerta, *ESAIM: Math. Modell. Numer. Anal.* **40**, 653 (2006).
- [16] F. Boyer, C. Lapuerta, S. Minjeaud, B. Piar, and M. Quintard, *Transp. Porous Media* **82**, 463 (2010).
- [17] C.-Y. Zhang, H. Ding, P. Gao, and Y.-L. Wu, *J. Comput. Phys.* **309**, 37 (2016).
- [18] H. Liu, Q. Kang, C. R. Leonardi *et al.*, *Comput. Geosci.* **20**, 777 (2016).
- [19] C. Xie, J. Zhang, V. Bertola, and M. Wang, *J. Colloid Interface Sci.* **463**, 317 (2016).
- [20] C. Xie, J. Zhang, V. Bertola, and M. Wang, *J. Non-Newtonian Fluid Mech.* **234**, 118 (2016).
- [21] H. Huang, M. Sukop, and X. Lu, *Multiphase Lattice Boltzmann Methods: Theory and Application* (John Wiley & Sons, New York, 2015).
- [22] H. Huang, J.-J. Huang, and X.-Y. Lu, *Comput. Fluids* **93**, 164 (2014).
- [23] L. Zhang, Q. Kang, J. Yao, Y. Gao, Z. Sun, H. Liu, and A. J. Valocchi, *Sci. China: Technol. Sci.* **58**, 1375 (2015).
- [24] J. Bao and L. Schaefer, *Appl. Math. Modell.* **37**, 1860 (2013).
- [25] S. Leclaire, M. Reggio, and J.-Y. Trépanier, *J. Comput. Phys.* **246**, 318 (2013).
- [26] H. Liang, B. C. Shi, and Z. H. Chai, *Phys. Rev. E* **93**, 013308 (2016).
- [27] C. Semperebon, T. Kruger, and H. Kusumaatmaja, *Phys. Rev. E* **93**, 033305 (2016).
- [28] D. Rothman and J. Keller, *J. Stat. Phys.* **52**, 1119 (1988).
- [29] A. K. Gunstensen, D. H. Rothman, S. Zaleski, and G. Zanetti, *Phys. Rev. A* **43**, 4320 (1991).
- [30] D. Grunau, S. Chen, and K. Eggert, *Phys. Fluids A* (1989–1993) **5**, 2557 (1993).
- [31] S. Leclaire, M. Reggio, and J.-Y. Trépanier, *Comput. Fluids* **48**, 98 (2011).
- [32] S. Leclaire, N. Pellerin, M. Reggio, and J.-Y. Trépanier, *Int. J. Multiphase Flow* **57**, 159 (2013).
- [33] S. Leclaire and N. Pellerin, *J. Phys. A: Math. Theor.* **47**, 105501 (2014).
- [34] T. N. Phillips and G. W. Roberts, *IMA J. Appl. Math.* **76**, 790 (2011).
- [35] L. Giraud, D. D’Humières, and P. Lallemand, *Europhys. Lett.* **42**, 625 (1998).
- [36] P. Lallemand, D. d’Humières, L.-S. Luo, and R. Rubinstein, *Phys. Rev. E* **67**, 021203 (2003).
- [37] A. J. Wagner, L. Giraud, and C. E. Scott, *Comput. Phys. Commun.* **129**, 227 (2000).
- [38] A. J. Wagner, *Prog. Comput. Fluid Dyn.* **5**, 20 (2005).
- [39] P. J. Dellar, *SIAM J. Sci. Comput.* **36**, A2507 (2014).
- [40] J. Onishi, Y. Chen, and H. Ohashi, *Prog. Comput. Fluid Dyn.* **5**, 75 (2005).
- [41] O. Malaspinas, N. Fiétier, and M. Deville, *J. Non-Newtonian Fluid Mech.* **165**, 1637 (2010).
- [42] F. Osmanlic and C. Körner, *Comput. Fluids* **124**, 190 (2016).
- [43] J. Onishi, Y. Chen, and H. Ohashi, *Physica A (Amsterdam, Neth.)* **362**, 84 (2006).
- [44] J. Su, J. Ouyang, X. Wang, and B. Yang, *Phys. Rev. E* **88**, 053304 (2013).
- [45] I. Ispolatov and M. Grant, *Phys. Rev. E* **65**, 056704 (2002).
- [46] M. Yoshino, Y. Toriumi, and M. Arai, *J. Comput. Sci. Technol.* **2**, 330 (2008).
- [47] T. Inamuro, T. Ogata, S. Tajima, and N. Konishi, *J. Comput. Phys.* **198**, 628 (2004).
- [48] Z. Guo, C. Zheng, and B. Shi, *Phys. Rev. E* **83**, 036707 (2011).

- [49] F. Jiang and T. Tsuji, *Water Resour. Res.* **53**, 11 (2017).
- [50] M. Sbragaglia, R. Benzi, L. Biferale, S. Succi, K. Sugiyama, and F. Toschi, *Phys. Rev. E* **75**, 026702 (2007).
- [51] M. Latva-Kokko and D. H. Rothman, *Phys. Rev. E* **72**, 046701 (2005).
- [52] H. Ding and P. D. Spelt, *Phys. Rev. E* **75**, 046708 (2007).
- [53] A. J. Ladd, *J. Fluid Mech.* **271**, 285 (1994).
- [54] A. J. Ladd and R. Verberg, *J. Stat. Phys.* **104**, 1191 (2001).
- [55] Y. J. Liu, T. Y. Liao, and D. D. Joseph, *J. Fluid Mech.* **304**, 321 (1995).
- [56] J. R. Herrera-Velarde, R. Zenit, D. Chehata, and B. Mena, *J. Non-Newtonian Fluid Mech.* **111**, 199 (2003).
- [57] X. Frank and H. Z. Li, *Phys. Rev. E* **74**, 056307 (2006).
- [58] S. B. Pillapakam, P. Singh, D. Blackmore, and N. Aubry, *J. Fluid Mech.* **589**, 215 (2007).
- [59] Y. Imaizumi, T. Kunugi, T. Yokomine, and Z. Kawara, *Chem. Eng. Sci.* **120**, 167 (2014).
- [60] S. L. Ortiz, J. S. Lee, B. Figueroa-Espinoza, and B. Mena, *Rheol. Acta* **55**, 879 (2016).
- [61] D. Fraggedakis, M. Pavlidis, Y. Dimakopoulos, and J. Tsamopoulos, *J. Fluid Mech.* **789**, 310 (2016).
- [62] X. Wu, C. Xiong, H. Xu *et al.*, SPE-177421-MS, 2015, <https://www.onepetro.org/conference-paper/SPE-177421-MS>.
- [63] A. Gunther and K. F. Jensen, *Lab on a Chip* **6**, 1487 (2006).
- [64] Z.-L. Guo, C.-G. Zheng, and B.-C. Shi, *Chin. Phys.* **11**, 366 (2002).
- [65] Q. Lou, Z. Guo, and B. Shi, *Phys. Rev. E* **87**, 063301 (2013).